Published in final edited form as:
Magn Reson Med. 2014 August ; 72(2): 438–445. doi:10.1002/mrm.24937.

Flow Compensated Quantitative Susceptibility Mapping for Venous Oxygenation Imaging

Bo Xu[1,2], **Tian Liu**[1,3], **Pascal Spincemaille**[1], **Martin Prince**[1], and **Yi Wang**[1,2,4,*]

[1]Department of Radiology, Weill Cornell Medical College, New York, New York, USA

[2]Department of Biomedical Engineering, Cornell University, Ithaca, New York, USA

[3]MedImageMetric LLC, New York, New York, USA

[4]Department of Biomedical Engineering, Kyung Hee University, Seoul, Korea

Abstract

Purpose—Venous blood oxygen saturation is an indicator of brain oxygen consumption and can be measured directly from quantitative susceptibility mapping (QSM) by deconvolving the MR phase signal. However, accurate estimation of the susceptibility of blood may be affected by flow induced phase in the presence of imaging gradient and the inhomogeneous susceptibility field gradient. The purpose of this study is to correct the flow induced error in QSM for improved venous oxygenation quantification.

Methods—Flow compensation is proposed for QSM by using a fully flow compensated multi-echo gradient echo sequence for data acquisition. A quadratic fit of the phase with respect to echo time is employed for the flow phase in the presence of inhomogeneity field gradients. Phantom and in vivo experiments were carried out to validate the proposed method.

Results—Phantom experiments demonstrated reduced error in the estimated field map and susceptibility map. Initial data in in vivo human imaging demonstrated improvements in the quantitative susceptibility map and in the estimated venous oxygen saturation values.

Conclusion—Flow compensated multi-echo acquisition and an adaptive-quadratic fit of the phase images improves the quantitative susceptibility map of blood flow. The improved vein susceptibility enables in vivo measurement of venous oxygen saturation throughout the brain.

Keywords

QSM; susceptibility; venous oxygen saturation; adaptive-quadratic fit

INTRODUCTION

Magnetic susceptibility is a physical tissue property that varies in healthy tissue and may also change with pathologic conditions. Susceptibility provides information complementary to traditional T1, T2, and T2* weighted images. Quantitative susceptibility mapping (QSM)

*Correspondence to: Yi Wang, Ph.D., 416 E 55th Street, New York, NY 10022. yw233@cornell.edu.

computes the magnetic susceptibility distribution based on the magnetic field inhomogeneity generated by magnetic sources (1–8). QSM has been shown to provide useful anatomical and clinical information for brain iron quantification (9,10), subthalamic nucleus visualization (11), and cerebral microbleeds characterization (12). Because magnetic susceptibility is linear in the deoxyhemoglobin concentration, it also allows venous oxygen saturation quantification (13–16).

However, blood flow induced artifacts hamper accurate measurement of blood susceptibility. QSM uses a dipole deconvolution of the magnetic field measured by MRI to obtain the susceptibility distribution. Typically, to compute the field map, multi-echo gradient echo phase images are acquired and the field map is estimated by performing a linear fit of the phase to the echo time (TE). However, in the presence of flow, usually between 10 and 20 cm/s in the veins (17,18) and local spatial field inhomogeneity, this linear assumption does not hold. Travelling spins accumulate additional phase that may cause vessel misalignment and erroneous magnetic field estimation. Without correction, the computed field map in vessels may not be accurate and may lead to unreliable blood susceptibility and oxygen saturation values.

In this study, the theoretic relationship between the phase, both in image space and k-space, of flowing spins and echo time (TE) is derived. A data acquisition and a reconstruction approach is proposed to improve the vessel susceptibility quantification. In the data acquisition, gradient moment nulling is added to the readout, phase and slice encoding directions for all echoes. In the data reconstruction, a quadratic fit is used for regions exhibiting flow while a linear fit is used for regions with static spins. Phantom experiments are performed to validate the theory and demonstrate the improved field map estimation. Improved image quality is demonstrated in human brain images. More consistent venous oxygen saturation measurement is achieved with the improved susceptibility value.

THEORY

Signal Modeling

The k-space MRI signal s at time *t* acquired for a static spin isochromat could be written as:

$$\mathrm{s}(t) = \int \rho(\mathbf{r})\, \mathrm{e}^{-i\left(\psi + \gamma \delta \mathrm{B}(\mathbf{r}) t + \gamma \int_0^t \mathbf{G}(\tau)\mathrm{d}\tau \cdot \mathbf{r}\right)} \mathrm{d}\mathbf{r}$$

where $\rho(\mathbf{r})$ is the density of the spin isochromats at position $\mathbf{r}$, ψ is an initial phase after the radio frequency (RF) pulse; γ is the gyromagnetic ratio; $\delta \mathrm{B}(\mathbf{r})$ is the field inhomogeneity; $\mathbf{G}(\tau)$ is the imaging field gradient at time $0<\tau<t$. When flow exists, the position vector $\mathbf{r}$ of the excited spins depends on *t* and should be noted as $\mathbf{r}(t)$. The signal equation becomes:

$$\begin{aligned} \mathrm{s}(t) &= \int \rho(\mathbf{r}(0))\, \mathrm{e}^{-\mathrm{i}\left(\psi + \gamma \int_0^t \delta \mathrm{B}(\mathbf{r}(\tau))\mathrm{d}\tau\right)} \mathrm{e}^{-\mathrm{i}\gamma \int_0^t \mathbf{G}(\tau)\cdot\mathbf{r}(\tau)\mathrm{d}\tau} \mathrm{d}\mathbf{r} \\ &= \int \rho(\mathbf{r}(0))\, \mathrm{e}^{-i\phi_1} \mathrm{e}^{-\mathrm{i}\phi_2} \mathrm{d}\mathbf{r} \end{aligned} \quad [1]$$

The first phase term $\phi_1=\psi+\gamma\int_0^t \delta \mathrm{B}\left(\mathbf{r}\left(\tau\right)\right)\mathrm{d}\tau$ represents the phase that a spin isochromat accumulates along the traveling path in image space. The second phase term $\phi_2=\gamma\int_0^t \mathbf{G}\left(\tau\right)\cdot\mathbf{r}\left(\tau\right)\mathrm{d}\tau$ contains the usual k-space encoding. Let us assume that, for a given spatial location **r**, the velocity **v**(**r**(τ)) is constant in a local region around **r** and is constant in time, up to at least the largest TE. Then $\mathbf{r}(\tau)=\mathbf{r}_0+\mathbf{v}(\mathbf{r}_0)\tau=\mathbf{r}_{\mathrm{TE}}+\mathbf{v}(\mathbf{r}_0)(\tau\text{-TE})$, where $\mathbf{r}_0=\mathbf{r}(0)$ and $\mathbf{r}_{\mathrm{TE}}=\mathbf{r}(\mathrm{TE})$. Let us further assume δB(**r**) is linearly varying in a small local region around the path of the moving spin, i.e., $\delta\mathrm{B}(\mathbf{r}+\mathrm{d}\mathbf{r})=\delta\mathrm{B}(\mathbf{r})+\nabla\delta\mathrm{B}(\mathbf{r})\cdot\mathrm{d}\mathbf{r}$. After substituting **r**(τ) into Eq. [1], Φ_1 and Φ_2 becomes

$$\begin{aligned}\Phi_1 &= \psi+\gamma\int_0^{TE}\delta\mathrm{B}\left(\mathbf{r}_{TE}+\mathbf{v}\left(\mathbf{r}_0\right)\left(\tau-TE\right)\right)\mathrm{d}\tau \\ &= \psi+\gamma\int_0^{TE}\left(\delta\mathrm{B}\left(\mathbf{r}_{TE}\right)+\left(\tau-TE\right)\mathbf{v}\left(\mathbf{r}_0\right)\cdot\nabla\delta\mathrm{B}\left(\mathbf{r}_{TE}\right)\right)\mathrm{d}\tau \\ &= \psi+\gamma\delta\mathrm{B}\left(\mathbf{r}_{TE}\right)TE-\tfrac{1}{2}\gamma\mathbf{v}\left(\mathbf{r}_0\right)\cdot\nabla\delta\mathrm{B}\left(\mathbf{r}_{TE}\right)TE^2\end{aligned} \quad [2]$$

$$\begin{aligned}\Phi_2 &= \gamma\int_0^{TE}\mathbf{G}\left(\tau\right)\cdot\left(\mathbf{r}_{TE}+\mathbf{v}\left(\mathbf{r}_0\right)\left(\tau-TE\right)\right)\mathrm{d}\tau \\ &= \gamma\mathbf{r}_{TE}\cdot\int_0^{TE}\mathbf{G}\left(\tau\right)\mathrm{d}\tau+\gamma\mathbf{v}\left(\mathbf{r}_0\right)\cdot\int_0^{TE}\mathbf{G}\left(\tau\right)\left(\tau-TE\right)\mathrm{d}\tau \\ &= 2\pi\mathbf{r}_{TE}\cdot\mathbf{k}\left(TE\right)+\gamma\mathbf{v}\left(\mathbf{r}_0\right)\cdot\mathbf{M}\left(TE\right)\end{aligned} \quad [3]$$

where **k**(TE) is the k-space position and **M**(TE) is the first moment of **G**(τ) at time TE.

In Eq. [2], the phase Φ_1 is a quadratic function of TE: The linear coefficient reflects the local field inhomogeneity, causing shift along the readout direction; The quadratic coefficient is proportional to the flow velocity and the gradient of the field inhomogeneity, referred to here as the inhomogeneity field gradient. This quadratic phase term is independent of phase encoding and its TE squared dependence may cause blurring along the readout direction. In Eq. [3], the second term can be compensated using gradient moment nulling for a given imaging gradient as in standard MRA (19–25).

Gradient Moment Nulling

A diagram of the three-dimensional multi-echo gradient echo (GRE) sequence with first moment nulling gradient is illustrated in Figure 1. The fully flow compensation can be realized using the following gradient constraints (*t*=0 at the peak of the RF, *t*=*nTE* at the nth echo center):

$$\int_0^{TE}G_x\left(t\right)dt=0,\int_0^{TE}G_x\left(t\right)tdt=0,\int_{nTE}^{(n+1)TE}G_x\left(t\right)dt=0,\int_{nTE}^{(n+1)TE}G_x\left(t\right)tdt=0,$$

$$\int_0^{TE}G_y(t)dt=k_y/\gamma,\ \int_{(n-1)TE}^{nTE}G_y(t)dt=0(n>1),\ \int_0^{nTE}G_y(t)(t-nTE)dt=0,$$

$$\int_0^{TE}G_z(t)dt=k_z/\gamma,\ \int_{(n-1)TE}^{nTE}G_z(t)dt=0(n>1),\ \int_0^{nTE}G_z(t)(t-nTE)dt=0.$$

In the readout direction, each echo is refocused, and flow compensation is naturally achieved at the center of each echo after inserting an appropriate moment nulling gradient before the first echo. In the phase encoding directions (k_y and k_z), the first moment of phase encoding gradient increases from one echo to the next by the amount of the phase encoding gradient area (k_y or k_z) times the echo spacing, so the same gradient moment nulling can be used for all later echoes except the first one.

Gradient moment nulling removes the extra phase $\gamma\mathbf{v}(\mathbf{r}_0)\cdot\mathbf{M}(\mathrm{TE})$ for each TE in a multi-echo sequence. Note that gradient moment nulling only corrects for the ghosting artifacts in the magnitude images. The reconstructed image still has an extra phase component $\frac{1}{2}\gamma\mathbf{v}(\mathbf{r}_0)$ due to the varying local field in which the moving spins travel.

High Order Fit of the Multi-echo Phase

In image space, and under the assumptions stated above, phase is a linear or quadratic function of TE depending on whether or not the spin is traveling. A linear fit $\Phi_1=\psi+L\mathrm{TE}$ and a quadratic fit $\Phi_1=\psi^*+L^*\mathrm{TE}+Q^*\mathrm{TE}^2$ were performed for each voxel. However, there is much greater noise amplification in the quadratic fit than the linear fit due to the increased unknowns. To improve the SNR, a mixing of linear and quadratic fits, referred to as adaptive-quadratic fit, was developed to ensure that the quadratic fit was only used in regions with flow. As indicated in Eq. [2], the field inhomogeneity $\gamma\delta B$ is the coefficient of the linear term L or L^*. In flow regions, L and L^* are distinctly different and Q^* is nonzero. Based on this, the field inhomogeneity was computed as the combination of the two fit results: $\gamma\delta B = (1 - w)L + wL^*$, using the weighting $w = 1\text{-}e^{-\alpha|(L-L^*)Q^*|\mathrm{TE}^3}$, with an empirically determined weighting factor $\alpha=10^{-4}$. The resulting field inhomogeneity map served as the input for nonlinear morphology enabled dipole inversion (8), a dipole deconvolution solver, to compute the susceptibility map.

METHODS

Flow Phantom Experiment

Two experiments were carried out to validate the proposed theory and the use of the adaptive-quadratic fit. A U-shaped vinyl tube connected to a pump was fixed inside a plastic box, which was filled with tap water and put inside the scanner. The pump generated a constant flow with known velocity. Both experiments were performed on a 3 Tesla (T) scanner (GE Signa HDxt).

In the first experiment, two scans were performed: the first scan with an unmodified product sequence where flow compensation was only applied to the readout direction (10 echoes, $\mathrm{TR/TE_{first}/TE_{last}}$ FA = 36.0/3.1/32.2 ms, = 20°, coronal field of view (FOV) = 25 cm, voxel size = 1 × 1 × 1 mm^3, bandwidth (BW) = ±62.5 kHz) and the second scan with the proposed sequence with flow compensation applied in all three directions for all echoes (6 echoes, $\mathrm{TR/TE_{first}/TE_{last}}$ 35.0/3.1/30.3 ms, FA = 20°, coronal FOV 25cm, voxel = size 1 × 1 × 1 × mm^3). The flow velocity was set to 60cm/s to the magnitude of quadratic term component

$\mathbf{v}\cdot\nabla\delta B$ to that observed in preliminary in vivo studies. This was repeated several times. Each time, the tap water inside the tube was replaced with a gadopentetate dimeglumine (Gd-DTPA, Magnevist, Bayer HealthCare) solution with different concentrations. Two QSM images were reconstructed, one with a linear and one with an adaptive-quadratic fitted field map. The measured susceptibility was compared with that from the reference QSM images reconstructed from a scan without flow.

A second experiment was performed to validate the polynomial phase expansion in Eq. [2]. For a given flow velocity, two data sets were acquired for two different Z shimming gradient to create a magnetic field that varies linearly along the B0 direction. The Z direction was chosen because it coincides with the principal direction of the flow in the straight parts of the U shaped tube. A quadratic fit was performed for each of the two acquisitions obtaining $\varphi_{shim1}(\mathbf{r}) = \psi_1(\mathbf{r}) + L_1(\mathbf{r})TE + Q_1(\mathbf{r})TE^2$ and $\varphi_{shim2}(\mathbf{r}) = \psi_2(\mathbf{r}) + L_2(\mathbf{r})TE + Q_2(\mathbf{r})TE^2$. Then, the following holds:

$$\begin{aligned} Q_2(\mathbf{r}) - Q_1(\mathbf{r}) &= -\tfrac{1}{2}\gamma\mathbf{v}(\mathbf{r})\cdot\nabla(\delta B_2(\mathbf{r}) - \delta B_1(\mathbf{r})) \\ &= -\tfrac{1}{2}\mathbf{v_z}(\mathbf{r})\,\partial(L_2(\mathbf{r}) - L_1(\mathbf{r}))/\partial_z, \end{aligned}$$

where B_1 and B_2 are the total magnetic field of the two scans. In this equation, we have used the fact that the difference between B_1 and B_2 is induced by the difference in the Z shim, such that the assumption of a spatially linearly varying field in Eq. [2] is satisfied. Then, the flow velocity along Z can then be obtained as follows:

$$\mathbf{v_z}(\mathbf{r}) = -2(Q_2(\mathbf{r}) - Q_1(\mathbf{r}))/(\partial(L_2(\mathbf{r}) - L_1(\mathbf{r}))/\partial_z)$$

The acquisition of the two data sets with differing Z shimming was repeated for a range of flow velocities between 28 cm/s to 62 cm/s. For each of the velocities, these two acquisitions were performed (Z shim difference 1400 Hz/m) as well as a two-dimensional phase contrast scan (TR/TE = 15/6 ms, FA = 10°, FOV = 25 cm, matrix size = 256 × 128, slice thickness = 5 mm, BW = ± 15.63 kHz, VENC = 100 cm/s, using an acquisition plane orthogonal to the straight parts of the U shaped vinyl tube).

In Vivo Study

This study was institutional review board approved and HIPPA-compliant. In N = 8 healthy volunteers (seven male, one female), the brain was imaged using an 8-channel head coil on a 3T scanner (GE Healthcare) after obtaining informed consent. Typical scan parameters were: axial scan, seven echoes, $TR/TE_{first}/TE_{last}$ = 48.2/3.7/43.8 ms, FA = 20°, FOV = 24 cm, voxel size = 0.7 × 0.7 × 0.7 mm^3, BW = ±62.5 kHz. All volunteers were scanned using the proposed fully flow compensated sequence. Both a linear fit and the proposed adaptive-quadratic fit were used to obtain a field map. Two QSM images were reconstructed using the respective field maps. Major veins were identified by an experienced reader in a Maximal Intensity Projections (MIPs) of a 15-mm-thick volume centered at the location of the boundary between the two hemispheres. The number of visualized cortical veins longer than 1cm was compared between the two reconstructions. Venous oxygen saturation SvO_2 was computed using $\chi_{blood} = Hct(1\text{-}SvO_2)\Delta_{\chi do}$ (16). Hematocrit (Hct) was assumed to be 0.4

and the susceptibility difference between fully deoxygenated blood and oxygenated blood $\Delta_{\chi do}$ was assumed to be 3.43 ppm (14,20,26). Here χ_{blood} was the measured susceptibility value on the QSM images. In each volunteer, several estimates of SvO_2 were obtained by taking the mean over a region of interest (ROI) in each of the six largest cortical veins identified above using both the linear and adaptive-quadratic fit. Next, for each volunteer, the average and standard deviation of these six SvO_2 estimates were computed and compared between the two fitting models. The mean SvO_2 across all selected cortical veins and all volunteers was also computed and compared. All comparisons were analyzed statistically using pair-wise two-tailed t-tests with a *P* value of 0.05 indicating statistical significance.

RESULTS

Flow Phantom Experiment

Shown in Figure 2 are the magnitude images and phase data acquired without (Fig. 2a) and with (Fig. 2b) phase encoding flow compensation (i.e., k_y and k_z). In Figure 2a, without flow compensation, displacement artifacts appear in the phase encoding direction, which increase with TE. Due to the artifacts, the phase of a voxel (for instance indicated by the arrow) inside the tube has a nonlinear relationship with TE. In Figure 2b, it can be seen that flow compensation markedly reduces these artifacts. However, the phase of a voxel inside the tube exhibits an approximately quadratic relationship as a function of TE. The absolute value of the linear coefficient, presumed to be proportional to the field inhomogeneity, is 12 times larger for the linear fit (−0.0695) as compared to the quadratic fit (−0.0057).

Figure 3a shows the QSM error image of the flowing contrast agent solution. The error image was obtained by subtracting the reference QSM acquired during zero flow from the QSM acquired during non-zero flow. Inside the tube, the error of the adaptive-quadratic fit was markedly reduced compared with that from the linear fit, especially in the two ROI regions. Figure 3b shows the linear regression of the measured susceptibility versus the reference susceptibility for five distinct contrast agent solutions. In both ROIs, adaptive-quadratic fit exhibits more accurate measurement compared with linear fit over all the concentrations.

Figure 4a is the Z direction velocity map derived from the second order fit coefficient of the two scans with varying Z shim gradients. Opposite signs of velocity were observed on the two sides of the U shaped tube as the flow changes signs in the Z direction. The velocity in the selected ROI (see Figure 4a) was measured in six experiments with varying flow, which was then compared with the reference velocity measured with a phase contrast scan as shown in Figure 4b. Good agreement was found between the two measurements, with a linear regression slope of 1.1 and R^2 of 0.99.

In Vivo Study

Figure 5a shows QSM MIPs of a 15-mm-thick sagittal slab centered at the location of the boundary between the two hemispheres. Both linear fit and adaptive-quadratic fit results are shown here. The adaptive-quadratic fit reconstruction greatly improves vessel appearance,

especially in cortical veins. Several small veins missing in the linear fit QSM were recovered by the adaptive-quadratic fit method. Some veins that appeared disjointed in the linear fit QSM were better visualized using the adaptive-quadratic fit. The conspicuity and the sharpness of several dim veins were improved.

In all eight volunteers, more cortical veins were visualized in the adaptive-quadratic fit QSM. Figure 5c shows the number of cortical veins visualized within the 15 mm sagittal MIP in each volunteer. For all cases, more cortical veins were observed and the percentage increase from adaptive-quadratic fit QSM is 37.3% ± 14.9% ($P < 0.001$). The average venous oxygen saturation of six cortical veins based on the susceptibility map is shown in Figure 5d. The mean measured SvO_2 value across all volunteers is 72.2% ± 4.1% for the adaptive-quadratic fit method and 93.1% ± 5.3% for the linear fit ($P < 0.001$). Previous studies measured the SvO_2 in a range of 50% to 75% (27–29). Thus, the mean SvO_2 value from the adaptive-quadratic fit QSM falls within this range while that of the linear fit QSM would appear to lead to overestimation. For each volunteer, the error bar indicated the standard deviation of SvO_2 value over the six cortical veins used for measuring. The standard deviations for the linear fit method ranged from 5% to 17%, compared with those of the adaptive-quadratic fit, which ranged from 3% to 6%.

DISCUSSION

The preliminary results in this study suggest that flow compensation by nulling the gradient moment and modeling the flow phase under the gradient of the inhomogeneity field can reduce flow artifacts in image and improve the accuracy of mapping of in vivo venous blood susceptibility. The flow artifacts in both image magnitude and phase from multi-echo GRE acquisition are markedly reduced by flow compensation. This flow compensated quantitative susceptibility mapping (QSM) method may provide a robust measurement of venous oxygen saturation in the brain, as the blood susceptibility is deoxyhemoglobin concentration times the molar susceptibility of deoxyhemoglobin. Previous approaches to MRI measurements of venous oxygen saturation rely on various assumptions on susceptibility distributions including distribution geometries (13,15,27–34). QSM has the potential to overcome these limitations and errors associated with these assumptions. Flow compensation using imaging gradient moment nulling and inhomogeneity field gradient phase modeling was shown to increase consistency in the estimation of paramagnetic deoxyhemoglobin concentration.

The accumulated phase of proton spin isochromats is determined by the magnetic field they experience. This field may include a spatial gradient term consisting of imaging gradient used for spatial encoding or inhomogeneity field gradient induced by susceptibility sources. The imaging gradient is spatially uniform with magnitude as high as tens of mT/m. The inhomogeneity field gradient may be small and spatially varying, depending on the susceptibility strength and distribution. In the presence of a field gradient, the phase of moving spins is a polynomial function of time, quadratic for constant flow, as well-known in phase contrast MRA. The nonlinear phase–time relationship can cause erroneous k-space encoding and may lead to vessel displacement in the phase encoding direction and blurring in the readout direction. In a multi-echo acquisition, this flow-induced displacement

increases with TE and needs to be compensated for consistent voxel fitting across echoes. Flow compensation can be achieved using gradient moment nulling. In this study, we added bipolar flow compensation gradients in both phase encoding directions before each echo. The maximum TE was kept approximately unchanged. Because the addition of the compensation gradients increased the minimal echo spacing, this meant that the total number of echoes was reduced. To see the effect of the lower number of echoes on the resulting field map, the variance of the fitted field frequency ω can be computed according to (35):

$$\sigma^2(\omega) = \sigma^2 \frac{\sum \rho_i^2}{\left(\sum \rho_i^2\right)\left(\sum \rho_i^2 t_i^2\right) - \left(\sum \rho_i^2 t_i\right)^2}$$

where σ is the noise level of the complex echo images and $\rho = \rho e^{-\frac{t_i}{T_2^*}}$ is the magnitude for the *i*-th echo. Assuming a constant noise level σ, TE_{min} = 4 ms, TE_{max} = 44 ms and T2* = 50 ms (36), reducing the number of echoes from 11 to 7 (as used in this study), σ(ω) increases by 20%, leading to a decreased signal to noise for the estimated field frequency ω.

The gradient of the tissue induced inhomogeneity field, although typically much smaller than the imaging gradient, also needs to be considered in multiple echo sequences that include long TEs. This inhomogeneity field gradient may vary in space with unknown magnitude, making it difficult to be compensated. Consequently, it may cause not only image blurring along the readout direction (dephasing effects on high k_x components) but also quantitative error in phase measurement (phase shift at $k_x = 0$), the quadratic phase–time relationship in Eq. [2].

The quadratic relationship induced by flow and the inhomogeneity field gradient was demonstrated in the phantom experiment. From Eq. [2], a linear fit of the phase Φ_1 will lead to an underestimation of the field when $\mathbf{v}\cdot\Delta\delta B > 0$ or to an overestimation of the field when $\mathbf{v}\cdot\Delta\delta B < 0$. For the phantom study, the field in ROI 1 decreases along the flow direction, leading to $\mathbf{v}\cdot\Delta\delta B < 0$ consistent with the overestimation of the field and susceptibility in Figure 3b (solid triangles). However, in ROI 2, the field increases along the flow direction, leading to $\mathbf{v}\cdot\Delta\delta B > 0$, consistent with the underestimation of the field and susceptibility in Figure 3b (hollow triangles). The difference in field estimates between the linear and the adaptive fit can be quite substantial as shown in Figure 2b. By fitting the phase data with inclusion of the flow-induced quadratic term, the susceptibility map (Fig. 3a) was improved. In the in vivo brain study, the condition $\mathbf{v}\cdot\Delta\delta B > 0$ was also observed for the cortical veins where SvO2 was measured, leading to an underestimation of the field and the venous susceptibility. This resulted in oxygen saturation values higher than the range of values reported in the literature (Fig. 5d). The susceptibility map quality improves using the quadratic fit (Figs. 5a and b), and correspondingly the mean estimated oxygen saturation falls within that range (Fig. 5d). The mean SvO_2 value of 72.2% is consistent with a previous study (34) conducted by Fan et al., using a linear fit of the phase data, provided a value for $\Delta_{\chi do}$ of 0.27 ppm (cgs units, or 3.43 ppm in SI units) is used, as discussed by the authors of that study. This value for $\Delta_{\chi do}$ is consistent with experimentally obtained estimates. Performing QSM with the adaptive-quadratic fit can also eliminate the need to

restrict the measurement of SvO_2 to those vessels whose phase evolution is sufficiently linear in TE, as done in (34).

In this work, we derived and applied a quadratic fit in the vessel voxels assuming a locally constant flow and a linearly varying field inhomogeneity in one TR interval. A nonconstant (pulsatile) flow may exist in the vessels and higher order spatial variations may exist in the inhomogeneity field, resulting in higher order terms to the phase–time relationship. When these terms become substantial, a higher order polynomial fit is needed and can be easily incorporated into the approach outlined here. As the number of fit parameter increases, the noise of the fitted parameter also increases. To maintain a high SNR in the estimated parameters, we may desire the linear fit for voxels known of having no flow. Automated image segmentation of regions of no flow is a difficult mathematical problem. Instead, we adopted an empirical weighted average of both linear and quadratic fits using a weighting determined by the magnitude of the second order coefficient for the quadratic fit (an indication of the flow magnitude) and the difference between the linear coefficients of the two fits (another indication for flow existence). Preliminary results here demonstrated the feasibility of this weighting scheme but it may be further improved.

CONCLUSIONS

By using a fully flow compensated multi-echo GRE sequence and an adaptive-quadratic fit of the phase images at all echoes, vessel visibility and susceptibility measurements are improved. This method significantly reduces the flow induced displacement artifacts and improves the field inhomogeneity estimation to ensure a more accurate dipole deconvolution for obtaining the susceptibility map. Improved vein susceptibility enables in vivo measurement of venous oxygen saturation in the brain.

Acknowledgments

Grant sponsor: NIH; Grant numbers: R01EB013443; R01NS072370; R21DK090690; R21CA152275; 1R43EB015293-01.

REFERENCES

1. Liu J, Liu T, de Rochefort L, et al. Morphology enabled dipole inversion for quantitative susceptibility mapping using structural consistency between the magnitude image and the susceptibility map. Neuroimage. 2012; 59:2560–2568. [PubMed: 21925276]
2. de Rochefort L, Liu T, Kressler B, Liu J, Spincemaille P, Lebon V, Wu J, Wang Y. Quantitative susceptibility map reconstruction from MR phase data using bayesian regularization: validation and application to brain imaging. Magn Reson Med. 2010; 63:194–206. [PubMed: 19953507]
3. Liu T, Spincemaille P, de Rochefort L, Kressler B, Wang Y. Calculation of susceptibility through multiple orientation sampling (COSMOS): a method for conditioning the inverse problem from measured magnetic field map to susceptibility source image in MRI. Magn Reson Med. 2009; 61:196–204. [PubMed: 19097205]
4. Schweser F, Sommer K, Deistung A, Reichenbach JR. Quantitative susceptibility mapping for investigating subtle susceptibility variations in the human brain. Neuroimage. 2012; 62:2083–2100. [PubMed: 22659482]
5. Shmueli K, de Zwart JA, van Gelderen P, Li TQ, Dodd SJ, Duyn JH. Magnetic susceptibility mapping of brain tissue in vivo using MRI phase data. Magn Reson Med. 2009; 62:1510–1522. [PubMed: 19859937]

6. Li W, Wu B, Liu C. Quantitative susceptibility mapping of human brain reflects spatial variation in tissue composition. Neuroimage. 2011; 55:1645–1656. [PubMed: 21224002]
7. Wharton S, Bowtell R. Whole-brain susceptibility mapping at high field: a comparison of multiple- and single-orientation methods. Neuroimage. 2010; 53:515–525. [PubMed: 20615474]
8. Liu T, Wisnieff C, Lou M, Chen W, Spincemaille P, Wang Y. Nonlinear formulation of the magnetic field to source relationship for robust quantitative susceptibility mapping. Magn Reson Med. 2013; 69:467–476. [PubMed: 22488774]
9. Schweser F, Deistung A, Lehr BW, Reichenbach JR. Quantitative imaging of intrinsic magnetic tissue properties using MRI signal phase: an approach to in vivo brain iron metabolism? Neuroimage. 2011; 54:2789–2807. [PubMed: 21040794]
10. Langkammer C, Schweser F, Krebs N, et al. Quantitative susceptibility mapping (QSM) as a means to measure brain iron? A post mortem validation study. Neuroimage. 2012; 62:1593–1599. [PubMed: 22634862]
11. Schafer A, Forstmann BU, Neumann J, Wharton S, Mietke A, Bowtell R, Turner R. Direct visualization of the subthalamic nucleus and its iron distribution using high-resolution susceptibility mapping. Hum Brain Mapp. 2012; 33:2831–2842. [PubMed: 21932259]
12. Liu T, Surapaneni K, Lou M, Cheng L, Spincemaille P, Wang Y. Cerebral microbleeds: burden assessment by using quantitative susceptibility mapping. Radiology. 2012; 262:269–278. [PubMed: 22056688]
13. Haacke EM, Tang J, Neelavalli J, Cheng YC. Susceptibility mapping as a means to visualize veins and quantify oxygen saturation. J Magn Reson Imaging. 2010; 32:663–676. [PubMed: 20815065]
14. Jain V, Abdulmalik O, Propert KJ, Wehrli FW. Investigating the magnetic susceptibility properties of fresh human blood for noninvasive oxygen saturation quantification. Magn Reson Med. 2012; 68:863–867. [PubMed: 22162033]
15. Fernandez-Seara MA, Techawiboonwong A, Detre JA, Wehrli FW. MR susceptometry for measuring global brain oxygen extraction. Magn Reson Med. 2006; 55:967–973. [PubMed: 16598726]
16. Weisskoff RM, Kiihne S. MRI susceptometry - image-based measurement of absolute susceptibility of MR contrast agents and human blood. Magn Reson Med. 1992; 24:375–383. [PubMed: 1569876]
17. Yamada K, Naruse S, Nakajima K, Furuya S, Morishita H, Kizu O, Maeda T, Takeo K, Shimizu K. Flow velocity of the cortical vein and its effect on functional brain MRI at 1.5T: preliminary results by cine-MR venography. J Magn Reson Imaging. 1997; 7:347–352. [PubMed: 9090589]
18. Becker G, Perez J, Krone A, Demuth K, Lindner A, Hofmann E, Winkler J, Bogdahn U. Transcranial color-coded real-time sonography in the evaluation of intracranial neoplasms and arteriovenous malformations. Neurosurgery. 1992; 31:420–428. [PubMed: 1407424]
19. Bernstein, MA.; King, KF.; Zhou, ZJ. Handbook of MRI pulse sequences. Academic Press; Boston: 2004. p. xxiip. 1017
20. Wang Y. Principles of magnetic resonance imaging: physics concepts, pulse sequences, and biomedical applications. CreateSpace Independent Publishing Platform. 2012:276.
21. Bernstein MA, Shimakawa A, Pelc NJ. Minimizing TE in moment-nulled or flow-encoded two- and three-dimensional gradient-echo imaging. J Magn Reson Imaging. 1992; 2:583–588. [PubMed: 1392252]
22. Slavin GS, Riederer SJ. Gradient moment smoothing: a new flow compensation technique for multi-shot echo-planar imaging. Magn Reson Med. 1997; 38:368–377. [PubMed: 9339437]
23. Nishimura DG, Jackson JI, Pauly JM. On the nature and reduction of the displacement artifact in flow images. Magn Reson Med. 1991; 22:481–492. [PubMed: 1812381]
24. Haacke EM, Lenz GW. Improving MR image quality in the presence of motion by using rephasing gradients. AJR Am J Roentgenol. 1987; 148:1251–1258. [PubMed: 3495155]
25. Butts K, Riederer SJ. Analysis of flow effects in echo-planar imaging. J Magn Reson Imaging. 1992; 2:285–293. [PubMed: 1627863]
26. Spees WM, Yablonskiy DA, Oswood MC, Ackerman JJH. Water proton MR properties of human blood at 1.5 Tesla: magnetic susceptibility, T-1, T-2, T-2* and non-Lorentzian signal behavior. Magn Reson Med. 2001; 45:533–542. [PubMed: 11283978]

27. Wright GA, Hu BS, Macovski A. 1991 I.I. Rabi Award. Estimating oxygen saturation of blood in vivo with MR imaging at 1.5 T. J Magn Reson Imaging. 1991; 1:275–283. [PubMed: 1802140]
28. Haacke EM, Lai S, Reichenbach JR, Kuppusamy K, Hoogenraad FGC, Takeichi H, Lin WL. In vivo measurement of blood oxygen saturation using magnetic resonance imaging: a direct validation of the blood oxygen level-dependent concept in functional brain imaging. Hum Brain Mapp. 1997; 5:341–346. [PubMed: 20408238]
29. Lu H, Ge Y. Quantitative evaluation of oxygenation in venous vessels using T2-relaxation-under-spin-tagging MRI. Magn Reson Med. 2008; 60:357–363. [PubMed: 18666116]
30. Golay X, Silvennoinen MJ, Zhou JY, Clingman CS, Kauppinen RA, Pekar JJ, van Zijl PCM. Measurement of tissue oxygen extraction ratios from venous blood T-2: increased precision and validation of principle. Magn Reson Med. 2001; 46:282–291. [PubMed: 11477631]
31. Oja JM, Gillen JS, Kauppinen RA, Kraut M, van Zijl PC. Determination of oxygen extraction ratios by magnetic resonance imaging. J Cereb Blood Flow Metab. 1999; 19:1289–1295. [PubMed: 10598932]
32. Bolar DS, Rosen BR, Sorensen AG, Adalsteinsson E. QUantitative Imaging of eXtraction of oxygen and TIssue consumption (QUIXOTIC) using venular-targeted velocity-selective spin labeling. Magn Reson Med. 2011; 66:1550–1562. [PubMed: 21674615]
33. Jain V, Langham MC, Wehrli FW. MRI estimation of global brain oxygen consumption rate. J Cereb Blood Flow Metab. 2010; 30:1598–1607. [PubMed: 20407465]
34. Fan AP, Benner T, Bolar DS, Rosen BR, Adalsteinsson E. Phase-based regional oxygen metabolism (PROM) using MRI. Magn Reson Med. 2012; 67:669–678. [PubMed: 21713981]
35. Kressler B, de Rochefort L, Liu T, Spincemaille P, Jiang Q, Wang Y. Nonlinear regularization for per voxel estimation of magnetic susceptibility distributions from MRI field maps. IEEE Trans Med Imaging. 2010; 29:273–281. [PubMed: 19502123]
36. Siemonsen S, Finsterbusch J, Matschke J, Lorenzen A, Ding XQ, Fiehler J. Age-dependent normal values of T2* and T2′ in brain parenchyma. AJNR Am J Neuroradiol. 2008; 29:950–955. [PubMed: 18272561]

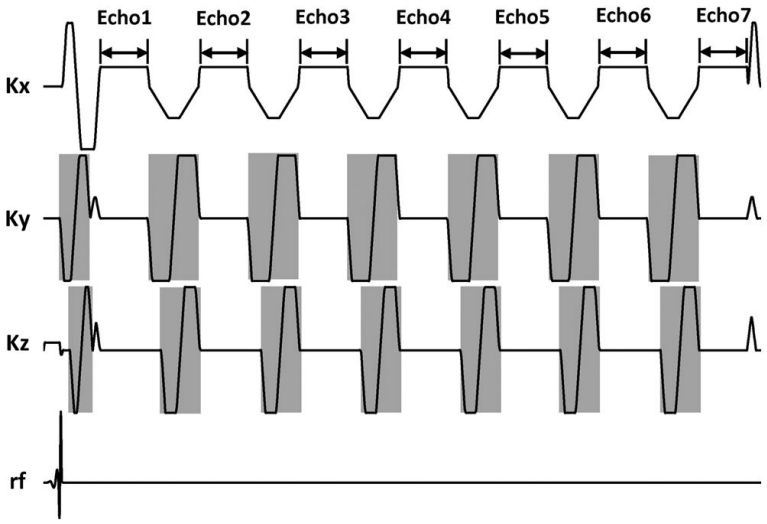

FIG. 1.

Pulse sequence diagram of the multi-echo fully flow compensated sequence. Bipolar flow compensation gradients (shaded in gray) are added before each echo in the phase and slice encoding directions to null the first order gradient moment.

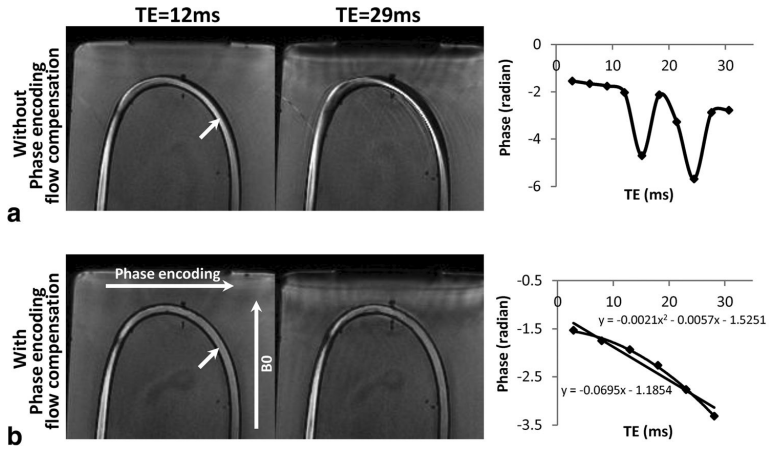

FIG. 2.

a,b: Comparison of multi-echo data without (a) and with (b) flow compensation in phase encoding directions. Shown are the magnitude images at TE = 12 ms and 29 ms and the phase-TE relationship of one voxel (pointed to by the white arrow). In (a), without flow compensation, water flow displacement artifacts appear in the phase encoding direction, which increase with TE. The phase measured in the later echoes no longer reflects the phase of the original voxel due to its flow-induced displacement. In (b), with flow compensation, the artifacts are substantially reduced. The phase of the same voxel exhibits an approximately quadratic relationship because of the of susceptibility induced field gradient. The absolute value of the linear coefficient (equal to $\gamma\delta B$ according to Eq. [2]) of the linear fit (−0.0695) is 12 times larger than that of the quadratic fit (−0.0057), indicating a substantial contribution of the flow induced quadratic term. Because of the increased minimum echo spacing when using flow compensation, the number of echoes in (b) is smaller.

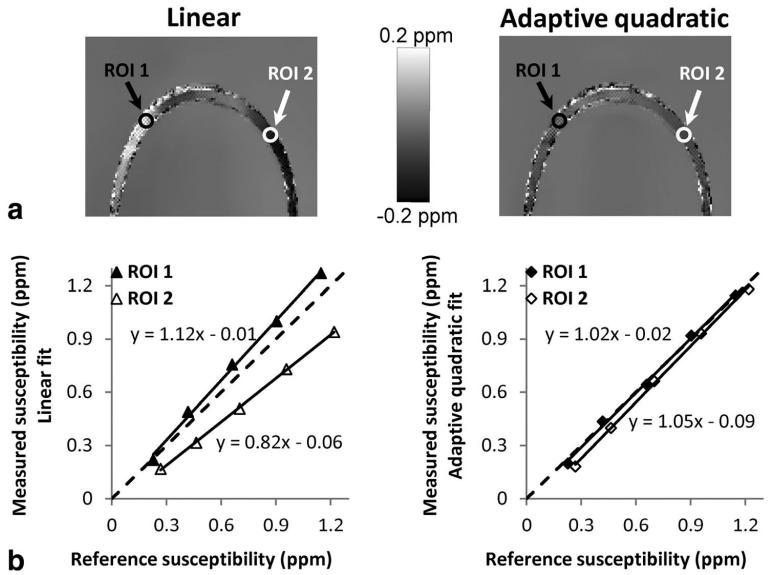

FIG. 3.

a: Error map of reconstructed susceptibility of flowing contrast agent solution at a velocity of 60 cm/s. Data were acquired with the fully flow compensated sequence. The reconstruction error using the adaptive-quadratic fit was markedly reduced compared with that using the linear fit, especially in regions pointed to by ROI1 and ROI2. **b:** Linear regression of the measured susceptibility versus the reference susceptibility. Five experiments with different concentration of contrast agent solutions were performed. The reference susceptibility was obtained in the zero-flow state. The measured susceptibility was obtained using both the linear and the adaptive-quadratic fit at a flow rate of 60 cm/s. Compared with the linear fit, the adaptive-quadratic fit exhibits more accurate measurement over all concentrations with a regression slope close to 1.

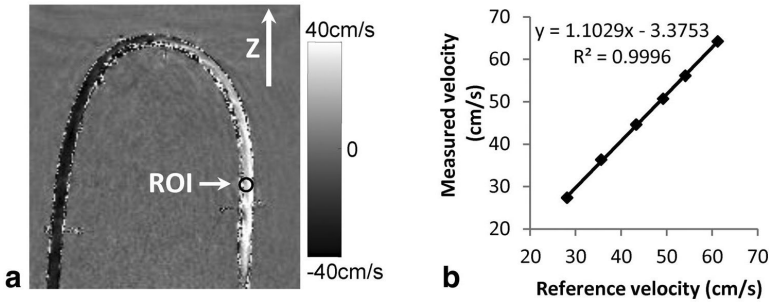

FIG. 4.

a: A representative Z direction flow velocity map computed based on the theory. Two data sets are acquired, which are identical except for a different Z shim gradient. The coefficients of the quadratic fit are used to obtain this velocity map. The estimated flow has opposite signs on the two straight sections, as expected. **b:** Linear regression of the measured flow velocity versus the reference flow velocity at six velocity settings. The obtained regression slope is 1.1 and R^2 is 0.99, indicating a good agreement of the measured velocity. The reference flow velocity was obtained using a separate phase contrast acquisition for each flow setting.

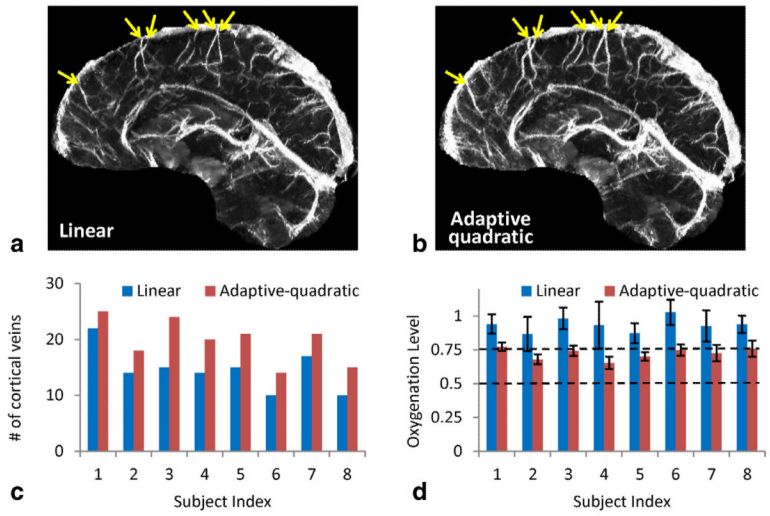

FIG. 5.

In vivo comparison of the linear and adaptive-quadratic fit. **a,b:** MIPs from linear (a) and adaptive-quadratic (b) fit QSM shows the improvement of the vessel depiction using the adaptive-quadratic fit. Dim and apparently disconnected veins from the linear fit result are better visualized using the adaptive-quadratic fit. **c:** Quantitative comparison of visualized cortical veins. In all subject, 37.3% ± 14.9% more cortical veins are visualized using the adaptive-quadratic fit. **d:** The measured venous oxygen saturation (SvO_2) from both the linear and adaptive-quadratic fit QSM in all volunteers. Arrows indicate the veins on which the measurements were performed. The value is 72.2% ± 4.1% for the adaptive-quadratic fit method and 93.1% ± 5.4% for the linear fit method. The SvO_2 variance over the six cortical veins for ROI analysis for each subject is also smaller for the adaptive-quadratic fit QSM (3–6%) compared with the linear fit QSM (5–17%).